Eur. Phys. J. D **31**, 179–188 (2004)
DOI: 10.1140/epjd/e2004-00155-6

THE EUROPEAN PHYSICAL JOURNAL D

Prospects for production of ultracold $X^1\Sigma^+$ RbCs molecules*

T. Bergeman[1,a], A.J. Kerman[2], J. Sage[2], S. Sainis[2], and D. DeMille[2]

[1] Department of Physics and Astronomy, SUNY, Stony Brook, NY 11794-3800, USA
[2] Department of Physics, Yale University, New Haven, CT, USA

Received 30 June 2004 / Received in final form 1st September 2004
Published online 23 November 2004 –

Abstract. Recently, we have reported photoassociation of laser-cooled Rb and Cs atoms, decay of the RbCs photoassociation resonances to high levels of the $a^3\Sigma^+$ state, and reexcitation to vibronic levels of the $c(2)^3\Sigma^+$ state [Kerman et al., Phys. Rev. Lett. **92**, 033004; 153001 (2004)]. Considering the reexcitation spectrum, we report here a preliminary analysis of perturbations in the c state by high levels of the $b^3\Pi$ and low levels of the $B^1\Pi$ state. Mixing with the B state provides the singlet character needed to stimulate decay to $v = 0$ of the $X^1\Sigma^+$ ground state. We conclude that an experimental procedure that involves photoassociation of laser-cooled atoms, radiative decay, and stimulated Raman transfer to the ground electronic state is a feasible method for producing translationally, rotationally, vibrationally and electronically cold RbCs molecules.

PACS. 33.80.Ps Optical cooling of molecules; trapping – 34.50.Gb Electronic excitation and ionization of molecules; intermediate molecular states (including lifetimes, state mixing, etc.) – 33.20.Kf Visible spectra – 34.20.-b Interatomic and intermolecular potentials and forces, potential energy surfaces for collisions – 33.15.Pw Fine and hyperfine structure

1 Introduction

Recently, there has been intense interest in the production of ultracold diatomic molecules. A number of laboratories have reported translationally and rotationally cold homonuclear diatomic molecules from the decay of photoassociation resonances [1–8] while others have used Feshbach resonance states [9–16]. Bose condensates [17,18] and Fermionic condensates [19] have been produced from these cold molecules. There has also been progress in the production of cold polar (heteronuclear) diatomic molecules using the above techniques [20–24]. With the exception of the report of tentative evidence for the production of K_2 molecules in the $v = 0$ level of the ground $X^1\Sigma_g^+$ state [4], these methods have not yet yielded molecules that are electronically and vibrationally as well as translationally and rotationally cold. The techniques of buffer gas cooling, which has been used for CaH [25], VO [26], and PbO [27], and electrostatic slowing, which has been achieved for beams of (metastable) CO [28], ND_3 [29], OH [30], and YbF [31] do yield cold molecules in the ground vibronic state. At present, molecular translation temperatures obtained with buffer gas loading and electrostatic slowing are not yet comparable to those achieved by laser cooling techniques. Other techniques that have shown promise include selection of the Boltzmann tail [32], condensation onto helium nanodroplets [33] and direct laser cooling of molecules [34].

Polar molecules have attracted interest because of special properties of condensates with interparticle dipolar interactions [35,36] and special behavior in external fields [37]. The particular motivation for work at Yale on the polar molecular species, RbCs, has been the goal of producing addressable qubits [38]. The cold polar molecules are to be placed in an optical lattice in the presence of a spatially varying electric field, so that due to the Stark effect, transition frequencies will depend on the position of the polar molecules in space. The prequisite for this scheme is the production of molecules that are vibrationally as well as rotationally cold, hence stable to collisional damping effects. Progress towards the goal of producing ultracold $v = 0$ RbCs molecules has now been reported in the form of photoassociation [23] and detection of products of decay of the photoassociation resonances [24]. We report here more detail on the reexcitation from levels populated by decay of the photoassociation resonances (PAR). The goal of this phase of the experimental work is to efficiently populate the ground vibrational level of the ground electronic state ($X^1\Sigma^+$) in one stimulated Raman step following the decay of an optimally chosen PAR (see Fig. 1). We will make use of information from the observed spectral transitions, combined

* A supplementary table (Tab. I) is only available in electronic form at `http://www.eurphysj.org`

[a] e-mail: `thbergeman@notes.cc.sunysb.edu`

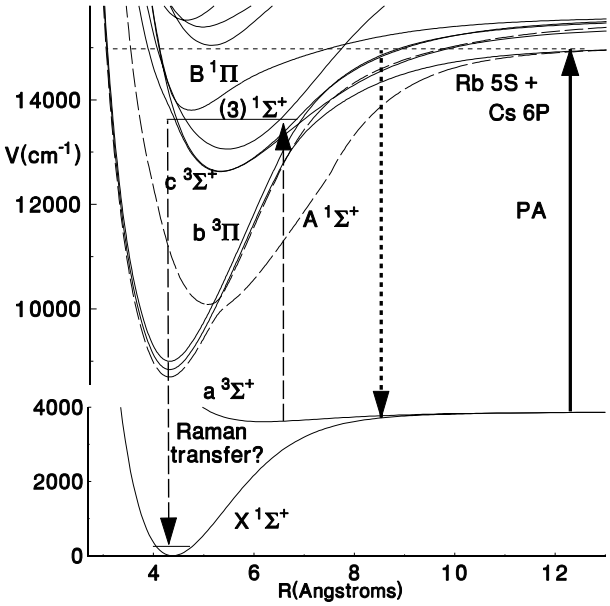

Fig. 1. Proposed scheme for populating the $v = 0$ level of the X state from photoassociation of Rb and Cs atoms: spontaneous decay to levels of the $a^3\Sigma^+$ state, reexcitation to a high level of the $c^3\Sigma^+$ state, followed by stimulated decay to $v = 0$ of the X state.

with results of ab initio calculations [39–41] to arrive at model potentials and spin-orbit coupling terms. This report will also discuss the gaps in our understanding of the molecular structure.

A general scheme of the proposed approach is shown in Figure 1 The zero of the energy scale in this figure and throughout the paper unless indicated otherwise is the minimum of the X state potential. We have given many of the electronic states letter names following customary usage for other alkali diatomic molecules.

As discussed in [24], reexcitation of the decay products of the photoassociation resonances has been interpreted as originating primarily from the $a^3\Sigma^+$ state. The most prominent transitions are to the $c^3\Sigma^+$ state, which was denoted the $(2)^3\Sigma^+$ state in reference [24]. To induce stimulated Raman decay to the $X^1\Sigma^+$ state, mixing with a singlet state is needed. Hence in this report, there will be special attention to mixing of upper levels of the c state with $B^1\Pi$ levels. Because the c state is also perturbed by the $b^3\Pi$ state, the level structure is complex and the observed transitions are only approximately assigned. We will lay out the available information and the analysis we have been able to perform to date.

In the following discussion, Section 2 outlines the experimental methods and Section 3 summarizes the observations. Section 4 presents our characterization of the a state, which is the lower state in all transitions discussed here. Section 5 outlines the Hamiltonian, the numerical methods, and the model form for the interatomic potentials for modeling the excited states and Section 6 summarizes the results of our analysis of the data on the c state and its perturbers. There is considerable attention to perturbations between the c and b states, but the primary interest is in the $c - B$ interaction, which makes it possible to stimulate decay to the singlet ground state.

2 Experimental techniques

The ^{85}Rb and ^{133}Cs atoms used for PA were collected and cooled in a dual-species, forced dark SPOT [42] magneto-optical trap (MOT) [23]. The atomic density n and atom number N were measured to be $n_{\rm Rb} = 7 \times 10^{11}$ cm^{-3}, $N_{\rm Rb} = 2 \times 10^8$, $n_{\rm Cs} = 1 \times 10^{12}$ cm^{-3}, $N_{\rm Cs} = 8 \times 10^8$ using two absorption imaging systems along orthogonal directions, with each probe beam containing both Rb and Cs resonant wavelengths. Independent measurements of N in which the trapping light was switched to resonance and the resulting transient fluorescence collected on a calibrated photodiode agreed to within 20%. The temperatures of both species were measured to be $\sim$75 μK, using time-of-flight absorption imaging.

The PA transition was driven by a Ti:sapphire laser producing $\sim$500 mW around 900 nm, just below the lowest atomic asymptote Rb $5S_{1/2}$ + Cs $6P_{1/2}$ (Fig. 1). This beam was focused onto the atomic clouds, with an e^{-2} waist size of $\sim$380 μm, producing an intensity sufficient to saturate the PA resonances used here. The frequency of this beam was actively locked to a previously observed PA resonance [23]; it was coupled into a Fabry-Perot optical spectrum analyzer, along with a fraction of the Rb trapping laser, which was used as a frequency reference. The optical spectrum was digitized in real time, and the relative peak locations were used as feedback to stabilize the laser frequency.

The ionization laser pulses were both of $\sim$7 ns duration, and were separated in time by $\sim$10 ns using a $\sim$3 m optical path difference. The first, resonant pulse had a tunable frequency in the near-infrared (IR), from 8350 $\rightarrow$ 10650 cm^{-1}, and a typical peak intensity of 3×10^8 W/m^2. It was generated using the output of a pulsed dye laser operating from 14000 $\rightarrow$ 18400 cm^{-1} at 10 Hz with pulse energies up to $\sim$20 mJ, and a spectral linewidth $\leq$0.05 cm^{-1}. This output was sent through a high pressure H_2 Raman cell (Light Age LAI 101 PAL-RC); for sufficiently high intensity, stimulated Raman scattering coherently produces additional frequency components offset by the H_2 vibrational splitting of 4155.25(5) cm^{-1} (by our own measurement). A dispersing prism was used to spatially separate the first or second Stokes (downshifted) Raman order, which was directed into the vacuum chamber. Its frequency was monitored using a wavemeter with 0.05 cm^{-1} absolute accuracy. The second, ionizing pulse was at 532 nm and had a typical intensity of 6×10^9 W/m^2; it was derived from the doubled Nd:YAG laser used to pump the dye laser.

Ions were detected using a channeltron (Burle 5901) biased at -2 kV, $\sim$3 cm from the atoms. A second electrode on the opposite side of the atoms was biased at +2 kV. The channeltron current was digitized during a 4 μs interval after each laser pulse using a 100 MHz data acquisition system (National Instruments PCI-5112), resulting in a time-of flight mass spectrum like that shown

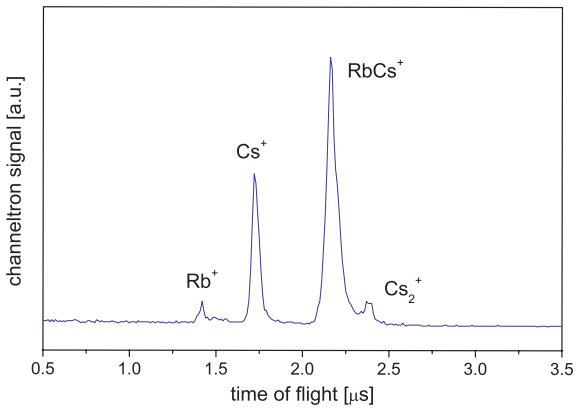

Fig. 2. Time of flight spectrum.

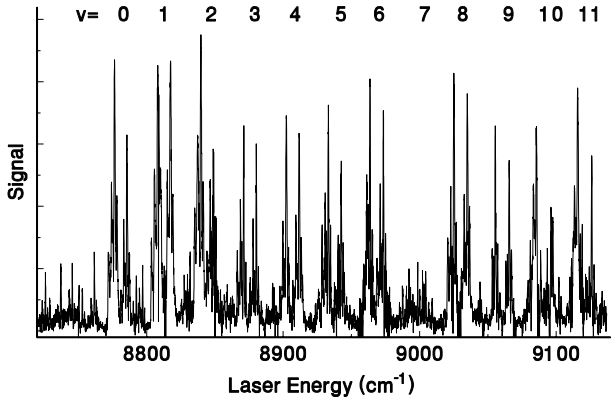

Fig. 3. Reexcitation spectrum showing predominant $a \rightarrow c$ transitions, each with c state $\Omega = 1$ and 0 components plus a state vibrational satellites. c state vibrational numbers are indicated at top. The horizontal scale is the energy of the laser photon. To obtain the energy of the upper state levels excited by the strongest a state vibrational component ($v = 37$), one must add the energy of the $v = 37$ level, which is 3831.18 ± 0.6 cm^{-1} above the minimum of the X state. We attribute the intensity minimum at $v = 7$ to a node in the Franck-Condon overlap.

in Figure 2. The $RbCs^+$ mass peak was observed only if both Rb and Cs atoms were trapped, *and* the PA laser was resonant with a suitable excited RbCs* level. The small Rb^+ and Cs_2^+ peaks in the spectrum arose respectively from the ionization of cold Rb atoms, and Cs_2 molecules produced by the trapping light (that is, independent of the PA laser) from cold Cs atoms. The larger Cs^+ peak resulted primarily from RbCs molecules via off-resonant multi-photon ionization [22] by the 532 nm pulse.

Bound-bound molecular spectra were obtained by stepping the frequency of the IR pulse, while recording the area under each mass peak. For each wavelength point, the time-of-flight mass spectrum was averaged over twenty shots of the pulsed laser. To ensure that we only detected RbCs molecules in their ground electronic manifold (the $a^3\Sigma^+$ or $X^1\Sigma^+$ electronic states), the PA laser was extinguished $\sim$100 μs before each ionizing pulse using a mechanical shutter, allowing any higher-lying electronic states ample time to decay. The intensities of the IR and 532 nm pulses were kept sufficiently low that neither by itself, nor the two in combination, produced $RbCs^+$ ions off-resonantly. Occasionally, however, resonant features were observed to result purely from the IR pulse, due to multiphoton processes. To prevent these from appearing in the spectrum, the 532 nm pulse was chopped off for every other shot using a shutter, and the mass spectra with and without it were subtracted for each frequency.

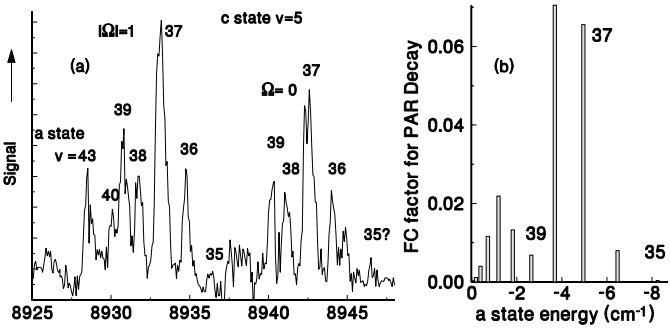

Fig. 4. (a) Detailed scans over the transition to the $v = 5$ level of the c state, showing the components from various a state vibrational levels. (b) Calculated Franck-Condon factors for decay of the 0^- photoassociation resonance 38 cm^{-1} below the $Cs(P_{1/2})$ threshold to various vibrational levels of the a state.

3 Observations

Initially, it was expected [23] that 0^+ photoassociation resonances would decay to high and moderately high vibrational levels of the ground $X^1\Sigma^+$ state, while 0^- PARs, which have negligible singlet character, would decay only to levels of the $a^3\Sigma^+$ state. (We recall that for $J = 0$ states below the Rb(5S) + Cs(6P) limit, the 0^+ manifold is composed of the $A^1\Sigma^+$ and $b^3\Pi_0^+$ states, while the 0^- channel involves the $c^3\Sigma_0^+$ component rather than $A^1\Sigma^+$.) Contrary to our expectation, the reexcitation spectra from both 0^+ and 0^- PARs exhibited a similar spectra of relatively weak transitions at low energy (such as those on the left end of Fig. 3 and shown more extensively in Fig. 2 of Ref. [24]) and then at higher energy, a robust series of vibronic bands that can be identified as $a \rightarrow c$ transitions, seen prominently in Figure 3. For each c state vibrational level, there are two rho-doublet components associated with $|\Omega| = 1$ (lower) and $\Omega = 0$, separated by about 9 cm^{-1} at low v. For each *component*, there is a series of peaks originating from shallow bound vibrational levels of the a state, with intensities that depend on the branching ratios for decay of the chosen photoassociation resonance. These will be referred to as "vibrational satellites". For $v = 5$ of the c state, the doublet components and the vibrational satellites are shown in Figure 4a from a scan in which the 0^- photoassociation resonance (PAR) 38 cm^{-1} below the Rb(5S) + $Cs(6P_{1/2})$ threshold was used, as is the case for all figures in this paper. The a state potential will be discussed further in the following section.

The strength of the $a \rightarrow c$ transitions is partly explained by relatively large Franck-Condon factors arising from the fact that inner wall of the a state lies just inside the R_e of the c state. It may be that for 0^+ PARs, observed reexcitation from the X state is weak because of the detection process as well as because of smaller Franck-Condon factors in the reexcitation step. From the a state, one expects also $a \rightarrow A/b$ transitions, and these are probably what appear before the onset of the $a \rightarrow c$ bands, as in Figure 3. Over a range of 400 cm^{-1} in laser energy, we have found about 16 transitions that exhibit a similar vibrational satellite structure as the $a \rightarrow c$ transitions. Three of these can be associated with transitions to known A/b upper levels, but the remainder are unidentified and do not exhibit expected $G(v)$ intervals. All available data [43,44] on the A and b states below the c state come from laser induced fluorescence of levels excited from the $X^1\Sigma^+$ state or from transitions from the $(4)^1\Sigma^+$ state to the A/b levels, each of which connect to levels of parity $(-1)^J$ (so-called e parity levels) and overwhelmingly favor $\Omega = 0$ levels of the b state. By contrast, excitation from the a state can also populate f parity states (total parity $-(-1)^J$) and $\Omega = 1$ and 2 levels, for which there is at present little information. Such states would have extremely weak transitions to X state levels, hence even if known, would not be of direct interest for producing cold X state molecules.

At higher energies, the regular $a \rightarrow c$ bands are perturbed by interactions first with the b state, and eventually with the B state. Figure 5 shows scan segments over various $a \rightarrow c$ bands from $c(v = 0)$ up to $c(v = 37)$ demonstrating a high degree of regularity of the upper state level structure up through c state $v = 30$. The vibrational satellites arising from transitions from different levels of the a state as in Figures 3 and 4 form a persistent pattern, as well as the rho-doubling interval, which varies slowly with v. Throughout these data scans, there are undoubtedly weaker $a \rightarrow A/b$ transitions from lower levels of the a state (below $v = 32$) transitions that are difficult to assign because of overlapping by lines of the dominant $a \rightarrow c$ sequence. However, we claim that there are unmistable effects of $c - b$ perturbations, as discussed below. Normally, when one studies perturbations in molecular spectroscopy, one has a series of rotational levels that exhibit an avoided crossing, for example. In this instance of excitation from cold molecules, rotational structure is not resolved, and the perturbation appears simply in the vibrational structure.

The scan segments in Figure 5 show that for transitions to c state levels above $v = 30$, there are extra lines beyond the $a \rightarrow c$ doublet and its vibrational satellites. One observes also shifts of the $a \rightarrow c$ transitions, and intensity borrowings. The $c^3\Sigma_0^+$ components are also shifted by coupling with $b^3\Pi_0$, but this is not shown in this display format in which all the $^3\Sigma_0^+$ peaks are vertically aligned. Although we cannot assign the extra lines in detail, we take the shifts and intensity patterns to indicate that the extra lines are not primarily from other band series, such as transitions from the X state. The data scans for $v = 31$ through 37 show an evolving sequence of additional peaks for which the intensities roughly correlate with the fraction of c state character in our (approximate) model. This is consistent with the hypothesis that the $a \rightarrow c$ transition amplitude is significantly stronger than the $a \rightarrow b$ transition amplitude, either due to the electronic factor or the vibrational overlap factors. Only when there is sufficient c state admixture do transitions to mostly b state levels become observable.

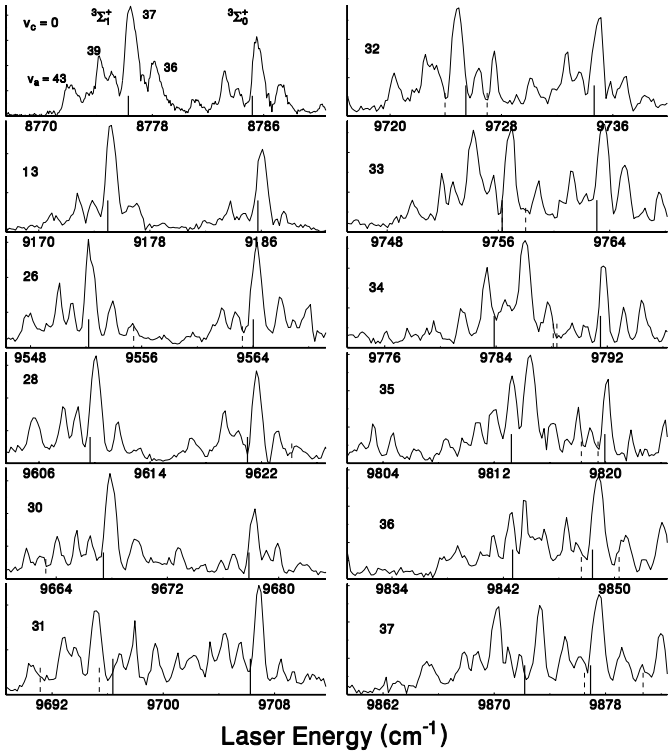

Fig. 5. Scans over various $a \rightarrow c$ bands with a uniform horizontal scale, and with the transitions to the $c^3\Sigma_0^+$ component aligned. Solid vertical lines denote transitions from $a(v = 37)$ to c state doublet components as calculated from the fitted potentials. Each scan exhibits the vibrational satellites that are shifted relative to the $v = 37$ transition as in Figure 4. In addition there are extra lines arising from transitions to $b^3\Pi_0$ and $^3\Pi_1$ levels that are identified only approximately. The calculated positions for transitions from $a(v = 37)$ are indicated with vertical dashed lines.

The first evidence of perturbation shifts occurs in the $v = 31$ band (Fig. 5), in which the $c^3\Sigma_1^+$ peak is displaced by about 1.4 cm^{-1} relative to the position interpolated from $v = 30$ and 32. A calculated $b^3\Pi_1$ peak (dashed vertical line) is located at the displaced position in our model. This is partly fortuitous, since we cannot reliably model the $b^3\Pi$ potential because of inadequate data. Scans at higher energies show a sharp decrease of the rho-doublet interval as well as extra lines, shifts and intensity anomalies.

Figure 6 shows observed lines close to the expected minimum of the B state. From the sequence of $a \rightarrow c$ transitions, it is evident that there is a discontinuity in the spacings, and we attribute that to effects of the B state.

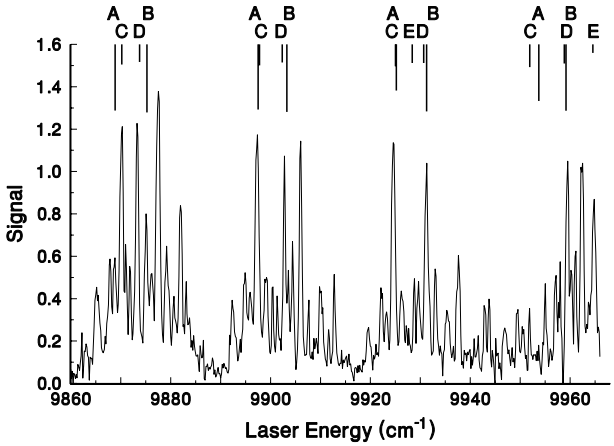

Fig. 6. This part of the reexcitation spectrum shows irregularities in the progression of $a^3\Sigma^+ \rightarrow c^3\Sigma^+$ transitions that we attributed to coupling with the $B^1\Pi$ state as well as the with the $b^3\Pi$ state. Here the letters A, B, C, D and E attached to the thick lines at the top denote calculated transitions to levels that are predominantly $^3\Sigma_1^+$,$^3\Sigma_0^+$,$^3\Pi_0$,$^3\Pi_1$, and $^1\Pi$, respectively. Clearly, the perturbation effects are not yet modeled quantitatively.

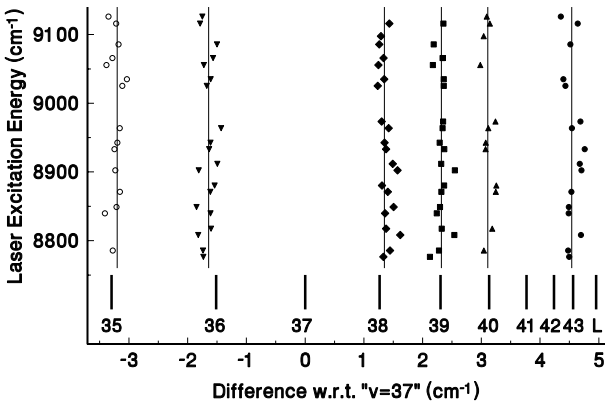

Fig. 7. Positions of the vibrational satellite peaks for various $a \rightarrow c$ bands, relative to the strongest peak, which has been tentatively assigned to $v = 37$. The thin vertical lines indicate the average values of these differences, while the thicker lines at the bottom are the positions of these peaks calculated from the a state potential discussed in the text. "L" = dissociation limit.

Quantitative understanding of coupling between the c and $B^1\Pi$ state requires first modeling the $b-c$ perturbations which begin to be seen about 270 cm^{-1} below the presumed onset of the B state. Although they are peripheral to the $B-c$ interaction, the main focus of this report, the $c-b$ interaction is a significant hurdle in our modeling efforts. We will now discuss the model for the a state and the excited states, and the fitting procedure.

4 The a state

Before presenting our analysis of the upper state level structure, we discuss the information available for the $a^3\Sigma^+$ state, since all transitions discussed here originate from a state levels. We have calculated a state eigenvalues using a potential constructed from the ab initio results of Allouche et al. [39], supplemented with the long range potential parameters obtained from the careful analysis of the X state potential by Fellows et al. [45]. The DVR numerical method [46,47], discussed below, was used to compute the eigenvalues of this single channel problem.

We have compiled the intervals between the vibrational satellites, such as those shown in Figure 4a, relative to the strongest one (tentatively assigned to $v = 37$) for $\approx$10 of the lowest $a \rightarrow c$ bands. The results are shown in Figure 7. The average values of these differences (thin vertical lines) agree well with the thick lines at the bottom of the figure, which represent eigenvalue differences calculated from the hybrid potential described above. Since it was not possible to unambiguously assign more deeply bound levels, and since no information on rotational structure was available, we were not able to optimize the a state potential beyond this original estimate. The resultant vibrational numbering, given in Figure 4, will be adopted in the following discussion although it is definitely tentative.

The $v = 37$ level of the a state is calculated to lie 4.96 ± 0.6 cm^{-1} below the Rb(5S) + Cs(6S) threshold, which is 3836.14 cm^{-1} above the minimum of the X state [45]. Figure 4b shows calculated Franck-Condon factors for decay from this same PAR to these high levels of the a state. Differences between these Franck-Condon factors and the observed line strengths indicate that our a state potential is not totally correct, hence uncertainties of ± 0.6 cm^{-1} are attached to the a state binding energies.

Transitions to very much higher c state vibrational levels produced a slightly different intensity distribution over the a state levels. Other photoassociation resonances yielded a different distribution of a state levels upon decay but were studied less extensively.

5 Analysis of data on excited states

5.1 Hamiltonian elements and numerical methods

The model Hamiltonian we employ is based on a diabatic basis of states of given S, Λ, and Ω, where S is the total spin. Λ and Ω are the projection of orbital and total angular momentum, respectively, along the internuclear axis [48]. The Hamiltonian is the sum of several terms: $H(R) = H_K + H_V(R) + H_{\rm so}(R) + H_{\rm rot}(R)$, and is a function of R, the internuclear distance. The kinetic energy operator, $H_K = -(\hbar^2/2\mu)\partial^2/\partial R^2$ is diagonal over the $^{2S+1}\Lambda_\Omega$ basis, but is represented by a full matrix over the discrete variable representation (DVR) mesh points [46,47]. $H_V(R)$ includes non-relativistic R-dependent potentials plus spin-independent relativistic effects, $H_{\rm so}(R)$ includes diagonal and off-diagonal spin-orbit interactions, and $H_{\rm rot}(R)$ expresses the effects of rotation,

which will be unimportant in this work. The non-zero matrix elements of $H_V(R) + H_{so}(R)$ are:

$$\langle {}^3\Pi_\Omega|H|{}^3\Pi_\Omega\rangle = V({}^3\Pi) + (\Omega - 1)\Delta_{bb} \quad (1)$$

$$\langle {}^3\Sigma^+_\Omega|H|{}^3\Sigma^+_\Omega\rangle = V({}^3\Sigma^+_\Omega) \quad (2)$$

$$\langle {}^1\Pi|H|{}^1\Pi\rangle = V({}^1\Pi) \quad (3)$$

$$\langle {}^3\Sigma^+_1|H|{}^1\Pi\rangle = \Delta_{cB} \quad (4)$$

$$\langle {}^3\Pi_1|H|{}^1\Pi\rangle = -\Delta_{bB} \quad (5)$$

$$\langle {}^3\Sigma^+_{|\Omega|}|H|{}^3\Pi_{|\Omega|}\rangle = \Delta_{cb}(\delta_{1,|\Omega|} + \sqrt{2}\delta_{\Omega,0}) \quad (6)$$

where the potential functions, $V({}^3\Sigma^+), V({}^1\Pi), V({}^3\Pi)$, and spin-orbit functions, Δ_{ij}, are functions of R. δ_{ij} is the Kronecker δ function and $H^\dagger = H$.

In the traditional band-by-band analysis of diatomic spectra, expectation values of $H_V(R)$ are obtained over vibronic wavefunctions such that the Hamiltonian parameters to be fitted are the vibronic energies, $G(v)$, rotational parameters, $B(v)$, centrifugal distortion parameters, and diagonal and off-diagonal spin-orbit terms, $A(v)$ and $\alpha(v, v')$. In this work as in other recent studies [43,49,50], we perform direct fits to the potentials and spin-orbit functions, by diagonalization of DVR matrices. The DVR method is similar to the Fourier grid Hamiltonian method [49,51] in that it produces an accurate representation of the kinetic energy and takes into account interactions among all coupled vibronic levels. Trigonometric basis functions result in equidistant mesh points [46]. A scaling function [47], $R = r_0/y^2 - r_s$, was used here to increase the density of mesh points at the potential minimum relative to the long range regime.

5.2 Model potentials and spin-orbit functions

For relatively shallow bound states, such as the RbCs c and B states, we have found that the modified Lennard-Jones (MLJ) potential of Hajigeorgiou and Le Roy [52] adequately expresses the expected long range behavior (we are not directly probing the long range states near the dissociation limit in this work) and also provides adequate parameters to adjust the short-range well. If the leading term of the potential is asymptotically known to be C_n/R^n, the MLJ potential is able to reproduce this asymptotic behavior by means of a potential of the form

$$V(R) = D_e\left[1 - \left(\frac{R_e}{R}\right)^n e^{-\beta_{MLJ}(z)z}\right]^2, \quad (7)$$

where D_e is the dissociation energy. $\beta_{MLJ}(z)$ is defined as

$$\beta_{MLJ}(z) = \sum_{m=0}^{M} \beta_m z^m. \quad (8)$$

To ensure the correct asymptotic form, the highest order term in z is chosen to be

$$\beta_M = \ln[2D_e(R_e)^n/C_n] - \sum_{m=0}^{M-1} \beta_M. \quad (9)$$

C_6 parameters for Rb(5S) + Cs(6P) atoms were taken from Marinescu and Sadeghpour [53]. The other MLJ parameters were initially obtained by least squares fit to an ab initio potential. As the experimental data obtained for this study included no rotational information, R_e values for the a, c and B states were initially fixed at the ab initio values. Later, R_e for the c state was adjusted from the ab initio value of 5.30 Å to 5.255 Å so that Franck-Condon factors calculated for transitions from $v = 37$ of the a state would exhibit a minimum at $v = 7$ of the c state, as in the experimental data shown in Figure 3 (other relative intensities in this figure reflect substantial saturation effects). This adjustment must be considered tentative because it is based on the tentative a state potential discussed above (Sect. 4). The $\beta_m (m \neq M)$ parameters for the c and B states were eventually adjusted by a fit to the experimental term value data. In calculating eigenvalues of the Hamiltonian, the rotational quantum number, J, was taken to be unity, ($J = 0$ would exclude levels of $\Omega = 1$, such as $c^3\Sigma_1$).

For the more deeply bound b and A states, the Dunham/RKR [54,55] expansion was used together with a polynomial interpolation to connect with the long range behavior of [53]. (For deeply bound state, the MLJ approach produced anomalous effects at small and/or large R.)

Relativistic (Hund's case c) potentials that include spin-orbit effects were reported in [40] and have been used at certain points in our work. However, near avoided crossings, the relativistic wavefunctions change rapidly with R, introducing non-adiabatic effects that are not well-known and are difficult to model in the fitting procedure. Hence we prefer to use case a "non-relativistic" potentials plus spin-orbit coupling functions to model the observed data. Thus representations of the large diagonal and off-diagonal spin-orbit functions are essential for accurately modeling the energy levels of RbCs. Although there have been many calculations of the analogous spin-orbit functions for other alkali dimers [50,51,56–58], ab initio spin-orbit functions are just beginning to become available for RbCs [41].

In every case in which diagonal or off-diagonal spin-orbit functions for heteronuclear or homonuclear alkali dimer states dissociating to the lowest S+P atomic limit have been calculated as a function of R, a significant dip has been found at an R value slightly greater than R_e [50,51,56–58]. This has been attributed [59] to reduction of the amplitude of the P atomic basis states in the molecular wavefunction as R decreases from ∞, before the rise of spin-orbit interactions as the united atom limit is approached. In view of this trend, and lacking more precise functional information, we have modeled each of the spin-orbit functions with Morse functions, normally used for diatomic potentials:

$$\Delta_i(R) = P_i(1) + [P_i(2) - P_i(1)]\left[1 - e^{\{P_i(3)[P_i(4)-R]\}}\right]^2. \quad (10)$$

The asymptotic limits of the spin-orbit functions, ($P_i(2)$ in the above expression) are known to be equal to one-third the atomic fine structure splitting, or that quantity times

$\sqrt{2}$ in the case of off-diagonal $\Omega = 0$ elements. The R value at minimum ($P_i(4)$), the minimum values ($P_i(1)$ above), and the width of the minimum ($P_i(3)$) are left to be adjusted to optimally fit the data. With this parametrization, reference [43] reported preliminary information on RbCs b state and the $A - b$ spin-orbit coupling functions. Improved results have been obtained more recently [44] (see Fig. 9 below).

6 Potentials and parameters for the c state and perturbers

Of the potentials displayed in Figure 1, all electronic states dissociating to Rb(5S) + Cs(6P) are appreciably coupled by the large spin-orbit functions. States dissociating to Rb(5P) + Cs(6S) are only weakly coupled to this manifold of states because the predominant electronic configuration differs by two orbitals. Of the latter manifold of states, the $(3)^1\Sigma^+$ state is calculated [40,39] to extend down even below the $B^1\Pi$ state that dissociates to Cs(6P), as shown in Figure 1. This state may contribute some small perturbation effects to states with $\Omega = 0^+$, but since it has not been accurately characterized from experimental data and since the coupling elements are presumably small, this state has been omitted in the analysis. The coupled states that we will be concerned with are therefore $c^3\Sigma^+$, $B^1\Pi$, $b^3\Pi$, and to a lesser extent, $A^1\Sigma^+$.

With the expanded Hamiltonian matrix, perturbation effects at higher v can be modeled to some extent. Spin-orbit functions couple components of equal Ω between the $c^3\Sigma_1^+, b^3\Pi_1$, and $B^1\Pi$ states. The information presently available on the b state consists of spectroscopic data [43,44] on perturbed $A^1\Sigma^+ - b^3\Pi_0$ levels up to 12,700 cm^{-1} above the minimum of the X state, corresponding to approximately $v = 3$ of the c state. The available information on $|\Omega| = 1$ components is very limited, and for $|\Omega| = 2$ components there is no information. More detailed potentials for the $|\Omega| = 1$ components of the b, c and B states for the region of special interest here are shown in Figure 8, as obtained from fits to the experimental data, while fitted spin-orbit functions are shown in Figure 9. Figure 8 shows potentials with and without off-diagonal spin-orbit effects included. For the low rotational levels ($J < 4$) observed here, the $|\Delta| = 1$ Coriolis coupling effects are negligible.

To a first approximation, values of the different spin-orbit elements can be related to each other by standard molecular-orbital theory [48]. For example, A_{Bb} is nominally equal to A_{bb}. For other alkali dimers [56–58], differences between these two functions have been found in ab initio calculations, but since no such results are presently available for RbCs, we will assume $A_{bb} = A_{Bb}$ here. We have obtained tentative fitted values for the other spin-orbit functions, as discussed below.

The measured energies, obtained from the laser energy at peak positions in the laser scan plus the energy of the $v = 37$ level of the a state as quoted above, were used to adjust the MLJ β_m potential parameters for the

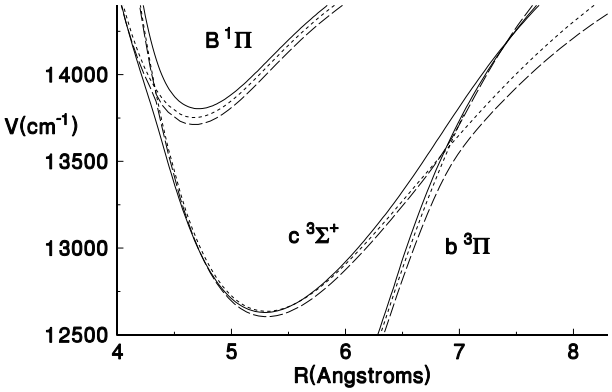

Fig. 8. Potential curves for the b, c and B states. Solid (short dashed) lines denote fitted (ab initio) non-relativistic potentials, long dashed lines are ab initio potentials with spin-orbit interactions.

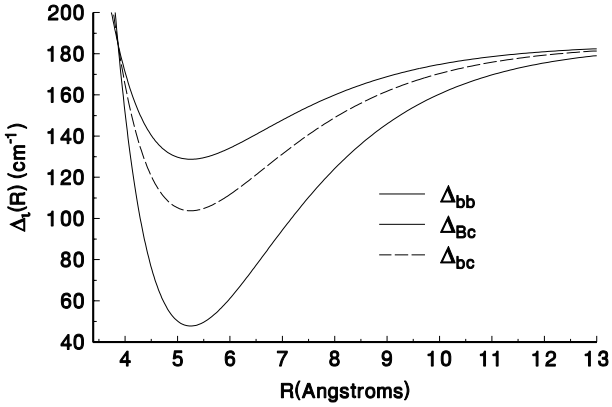

Fig. 9. Spin-orbit functions fitted from RbCs spectroscopic data.

c state, and to fit the spin-orbit interaction functions. Table 1 gives T_e, R_e, and ω_e values for the two c state components as well as for the $B^1\Pi$ state, from a fit that included spin-orbit coupling functions (among states dissociating to Rb(5S) + Cs(6P)). It also gives T_e and ω_e for the c state components deduced simply from the observed band positions, with no deperturbation process. Table 2 gives the observed energies, and energies calculated from the fitted potentials, of a few representative levels of low, intermediate and high v. A more complete listing is available in the supplementary *Online Material* (Tab. I). These listings show that up to the perturbation region, most observed c state levels are fit to an accuracy of about 0.3 cm^{-1} or better (apart from the 0.6 cm^{-1} absolute uncertainty in the position of the $v = 37$ a state level). Above energies of about 13500 cm^{-1} ($v = 31$), residuals in the fit increase, reflecting the fact that the perturbations are presently not accurately modeled.

The spin-orbit functions shown in Figure 9 are obtained from the perturbation shifts as well as from "extra lines" in the $a \rightarrow c$ spectrum and are constrained by the Morse function parametrization. The large R limits are from the well-known atomic fine structure intervals. For small values of R, it is difficult to estimate the uncertainty

Table 1. Parameters for the $c^3\Sigma_1^+, c^3\Sigma_0^+$, and $B^1\Pi$ states as compared with ab initio results of reference [40]. T_e and ω_e are in cm^{-1}, R_e is in Angstroms. The "partially deperturbed" values are obtained from fitting with a Hamiltonian matrix that includes off-diagonal spin-orbit interaction functions. The R_e values for the c state were obtained by matching $a \rightarrow c$ Franck-Condon factors with observed intensities, as discussed in the text.

	$c^3\Sigma_1^+$	$c^3\Sigma_0^+$	$B^1\Pi$
ab initio results of reference [40]			
T_e	12635.0	12636.0	13743.0
R_e	5.325	5.31	4.616
ω_e	29.1	32.2	40.8
This work — direct fit to *G(v)*			
T_e	12591.9(2)	12600.9(2)	
ω_e	31.8	31.8	
This work — partially deperturbed			
T_e	12584.5(2)	12588.8(2)	13736.3(6)
R_e	5.255	5.255	4.672
ω_e	32.1	31.6	36.1

of these curves, which must be regarding as preliminary at this point. The smallest minimum occurs in the function that couples $B^1\Pi$ and $c^3\Sigma_1^+$, and this is substantially smaller than the minimum of the other functions. We note that the relativistic potential curves of [40] exhibit an extremely small avoided crossing between the $^1\Pi$ and $^3\Sigma_1^+$ curves, which also suggests that in this region of $R \approx 4.5$ Å, the $B - c$ coupling is small.

For the lower vibrational levels of the c state, the splitting between the lower ($\Omega = 1$) and upper ($\Omega = 0$) component (ρ-doubling) varies slowly with v, as is evident from the scans in Figure 5, hence they can be modeled by different T_e and ω_e values for the two components. One can also attempt to explain this splitting by spin-orbit interactions with other states in the Hamiltonian manifold. Since the B state lies above the lowest 35 c state levels, $B - c$ spin-orbit coupling lowers the $c^3\Sigma_1^+$ components of these lower c state levels, but does not affect the $\Omega = 0$ components. The predominant $c - b$ interactions are those with b state levels below the c state levels (because of the Franck-Condon overlap factors), so both Ω components are raised by $c - b$ spin-orbit coupling. However, as seen in equation (6), the $\Omega = 0$ spin-orbit coupling element is $\sqrt{2}$ times larger than the $\Omega = 1$ element. Therefore the $c - b$ interactions also raise the c state $\Omega = 0$ levels relative to the $\Omega = 1$ elements. Thus, by expanding the Hamiltonian matrix to include the B and b states, part of the observed ρ-doubling of the c state can be explained. The ρ-doubling interval is about 9.0 cm^{-1} at low v, as seen from the "non-deperturbed" values in Table 1. From the partially deperturbed fit results given in Table 1, the residual difference in the c state T_e values is 4.3 cm^{-1}. In other fit results, including levels at higher energy, the residue ΔT_e can be as small as 2 cm^{-1}. These residual splitting values could arise from spin-orbit couplings with

Table 2. Representative values for observed energies, differences with calculated energies (in cm^{-1}), and calculated fractional compositions. "$|\Omega|$" identifies the level as either $^3\Sigma_\Omega^+$ or $^3\Pi_\Omega$, (the fractional compositions indicate which) and v gives the vibrational quantum number of the assigned symmetry.

Obs Term	Diff. Obs-Calc	$\|\Omega\|$	v	$^3\Sigma_\Omega^+$	$^3\Pi_\Omega$	$^1\Pi$
12607.59	−0.28	1	0	0.997	0.003	0.000
12616.69	0.15	0	0	0.995	0.005	
12639.41	−0.19	1	1	0.997	0.003	0.000
12648.61	−0.06	0	1	0.994	0.006	
12670.91	−0.02	1	2	0.996	0.004	0.000
12680.01	0.11	0	2	0.994	0.006	
12702.25	0.07	1	3	0.996	0.004	0.000
12711.49	0.02	0	3	0.994	0.006	
12733.50	0.03	1	4	0.996	0.004	0.000
12742.90	−0.15	0	4	0.993	0.007	
...	...	.	..	...	...	...
13135.74	−0.15	0	17	0.980	0.020	
13153.45	−0.29	1	18	0.983	0.017	0.000
13165.03	−0.14	0	18	0.979	0.021	
13182.46	−0.26	1	19	0.980	0.019	0.000
13194.19	−0.09	0	19	0.976	0.024	
13211.33	−0.17	1	20	0.978	0.022	0.000
13240.25	−0.20	1	21	0.975	0.024	0.001
13252.29	−0.10	0	21	0.972	0.028	
13269.02	−0.13	1	22	0.972	0.028	0.001
13280.81	0.28	0	22	0.969	0.031	
13297.53	0.15	1	23	0.968	0.031	0.001
13309.83	0.07	0	23	0.966	0.034	
13326.39	0.06	1	24	0.964	0.035	0.001
13338.37	0.25	0	24	0.963	0.037	
...	...	.	..	...	...	...
13566.14	−0.03	0	32	0.925	0.075	
13585.44	−0.18	1	33	0.906	0.091	0.003
13587.03	0.67	0	114	0.216	0.784	
13594.67	−0.34	0	33	0.919	0.081	
13614.54	−0.47	1	34	0.898	0.099	0.003
13622.90	−0.40	0	34	0.913	0.087	
13644.47	1.01	0	116	0.240	0.760	
13651.25	−0.62	0	35	0.907	0.093	
13674.79	−0.99	0	117	0.252	0.748	
13679.99	−1.26	0	36	0.900	0.100	
13701.38	0.37	0	118	0.264	0.736	
13704.44	0.90	1	114	0.230	0.762	0.008
13708.63	−1.84	0	37	0.893	0.107	
13728.47	0.88	0	119	0.275	0.725	
13733.94	−0.05	1	115	0.237	0.755	0.008
13737.18	−2.37	0	38	0.885	0.115	
13755.76	0.81	0	120	0.287	0.713	
13762.37	0.42	0	39	0.878	0.122	
13790.61	0.11	0	40	0.871	0.129	
13796.13	−0.04	1	1	0.128	0.023	0.849

Table 3. Calculated Franck-Condon factors based only on the $B^1\Pi$ component of the mixed $c-b-B$ wavefunctions, for various upper state levels near the minimum of the $B^1\Pi$ state.

Energy	Fractions			FC Factors $\times 10^4$	
(cm^{-1})	$^3\Pi_1$	$^1\Pi$	$^3\Sigma_1^+$	$X(v=0)$	$X(v=1)$
13618.25	0.788	0.007	0.205	1.0	0.3
13676.55	0.770	0.007	0.222	1.1	0.3
13700.43	0.124	0.008	0.868	1.1	2.5
13705.33	0.762	0.008	0.230	1.1	0.2
13733.89	0.755	0.008	0.238	1.3	0.3
13756.75	0.100	0.295	0.605	65.7	202.8
13759.90	0.040	0.716	0.244	125.1	408.1
13796.09	0.023	0.849	0.128	8.6	16.9
13814.07	0.135	0.152	0.714	14.9	40.5
13830.16	0.045	0.728	0.227	76.8	245.2

states outside our Hamiltonian matrix, but undoubtedly also reflect inaccuracies of our fitted spin-orbit coupling functions.

At higher energies, the pattern of $a \rightarrow c$ transitions is disrupted more drastically due to perturbations with the $B^1\Pi$ state, which is of crucial importance for inducing transitions to the $X^1\Sigma^+$ ground state. As seen in Figure 6, there is a discontinuity in the progression of $a \rightarrow c$ bands near laser excitation energy of 9950 cm^{-1} (energies of 13780 cm^{-1} relative to the minimum of the X state). This discontinuity occurs close to the minimum of the $B^1\Pi$ state predicted in ab initio calculations [39]. According to our model, observed $c^3\Sigma_1^+$ vibronic levels in this region have a significant amount of $B^1\Pi$ character. The calculated Franck-Condon overlaps with $v=0$ of the X state, taking into account only the $B^1\Pi$ part of the wavefunction, are given in Table 3. We hope to be able to detect cases in which the Franck-Condon factor is as small as 10^{-4}. As indicated in the table, several cases with adequate fraction of $c^3\Sigma_1^+$ character offer Franck-Condon factors, defined in this manner, of more than 50 times this magnitude. This has encouraged us to attempt experiments to stimulate decay of c state levels to $v=0$ and 1 of the X state by resonant laser light. Results of these efforts, which will be reported elsewhere, have been promising, leading us to believe that the route PAR $\rightarrow a \rightarrow c/B \rightarrow X(v=0)$ will produce adequate numbers of translationally, rotationally, vibrationally and electronically cold polar molecules that are the goal of this phase of our work.

In summary, our molecular structure model includes non-relativistic Born-Oppenheimer potentials and spin-orbit coupling functions that depend on R. Its application to the problem at hand is limited by inadequate data on rotational structure and on $b^3\Pi$ levels in the area of interest, which makes assignments in the region of the $c-b-B$ perturbations somewhat uncertain. Nevertheless, this model appears to be adequate for our present goals, namely to design a method to produce $v=0$ ultracold RbCs molecules.

We gratefully acknowledge support from NSF grant DMR-0325580, the David and Lucile Packard Foundation and the W. M. Keck Foundation for the work at Yale, and ONR, and NSF grant PHY-0354211, for support of the work at Stony Brook. Also, we thank C. Fellows and S. Kotochigova for valuable communications.

References

1. A. Fioretti, D. Comparat, A. Crubellier, O. Dulieu, F. Masnou-Seeuws, P. Pillet, Phys. Rev. Lett. **80**, 4402 (1998)
2. T. Takekoshi, B.M. Patterson, R.J. Knize, Phys. Rev. A **59**, R5 (1999)
3. R. Wynar, R. Freeland, D. Han, C. Ryu, D. Heinzen, Science **287**, 1016 (2000)
4. A. Nikolov, J. Ensher, E. Eyler, H. Wang, W. Stwalley, P. Gould, Phys. Rev. Lett. **84**, 246 (2000)
5. F. Fatemi, K. Jones, P. Lett, E. Tiesinga, Phys. Rev. A **66**, 053401 (2002)
6. C. Gabbanini, A. Fioretti, A. Lucchesini, S. Gozzini, M. Mazzoni, Phys. Rev. Lett. **84**, 2814 (2000)
7. C.M. Dion, C. Drag, O. Dulieu, B. Laburthe Tolra, F. Masnou-Seeuws, P. Pillet, Phys. Rev. Lett. **86**, 2253 (2001)
8. J. Léonard, M. Walhout, A. Mosk, T. Müller, M. Leduc, C. Cohen-Tannoudji, Phys. Rev. Lett. **91**, 073203 (2003)
9. C. Chin, A.J. Kerman, V. Vuletić, S. Chu, Phys. Rev. Lett. **90**, 033201 (2003)
10. E.A. Donley, N. Claussen, S. Thompson, C. Wieman, Nature **417**, 529 (2002)
11. C.A. Regal, C. Ticknor, J.L. Bohm, D.S. Jin, Nature **424**, 47 (2003)
12. J. Herbig, T. Kraemer, M. Mark, T. Weber, C. Chin, H.-C. Nägerl, R. Grimm, Science **301**, 1510 (2003)
13. K.E. Strecker, G.B. Partridge, R.G. Hulet, Phys. Rev. Lett. **91**, 080406 (2003)
14. K. Xu, T. Mukaiyama, J. Abo-Shaeer, J. Chin, D. Miller, W. Ketterle, Phys. Rev. Lett. **91**, 210402 (2003)
15. S. Jochim, M. Bartenstein, A. Altmeyer, G. Hendl, C. Chin, J. Hecker Denschlag, R. Grimm, Phys. Rev. Lett. **91**, 240402 (2003)
16. S. Dürr, T. Volz, A. Marte, G. Rempe, Phys. Rev. Lett. **92**, 020406 (2004)
17. M.W. Zwierlein, C. Stan, C. Schunck, S. Raupach, S. Gupta, Z. Hadzibabic, W. Ketterle, Phys. Rev. Lett. **91**, 250401 (2003)
18. S. Jochim, M. Bartenstein, A. Altmeyer, G. Hendl, S. Riedl, C. Chin, J. Hecker Denschlag, R. Grimm, Science **302**, 2101 (2003)
19. M. Greiner, C. Regal, D. Jin, Nature **426**, 537 (2003)
20. J.P. Shaffer, W. Chalupczak, N.P. Bigelow, Phys. Rev. Lett. **82**, 1124 (1999)
21. H. Wang, Bull. Am. Phys. Soc. **48**, J1.025 (2003)
22. M.W. Mancini, G.D. Telles, A.R.L. Caires, V.S. Bagnato, L.G. Marcassa, Phys. Rev. Lett. **92**, 133203 (2004)
23. A.J. Kerman, J.M. Sage, S. Sainis, T. Bergeman, D. DeMille, Phys. Rev. Lett. **92**, 033004 (2004)
24. A.J. Kerman, J.M. Sage, S. Sainis, T. Bergeman, D. DeMille, Phys. Rev. Lett. **92**, 153001 (2004)
25. J. Weinstein, R. deCarvalho, T. Guillet, B. Friedrich, J. Doyle, Nature **395**, 148 (1998)
26. J. Weinstein, R. deCarvalho, K. Amar, A. Boca, B. Odom, B. Friedrich, J. Doyle, J. Chem. Phys. **109**, 2656 (1998)

27. D. Egorov, J. Weinstein, D. Patterson, B. Friedrich, J. Doyle, Phys. Rev. A **63**, 030501 (2001)
28. H. Bethlem, G. Berden, G. Meijer, Phys. Rev. Lett. **83**, 1558 (1999)
29. H. Bethlem, F. Crompvoets, R. Jongma, S. van de Meerakker, G. Meijer, Phys. Rev. A **65**, 053416 (2002)
30. J. Bochinski, E. Hudson, H. Lewandowski, G. Meijer, J. Ye, Phys. Rev. Lett. **91**, 243001 (2003)
31. M. Tarbutt, H. Bethlem, J. Hudson, V. Ryabov, V. Ryzhov, B. Sauer, G. Meijer, E. Hinds, Phys. Rev. Lett. **92**, 173002 (2004)
32. S. Rangwala, T. Junglein, T. Rieger, P. Pinkse, G. Rempe, Phys. Rev. A **67**, 043406 (2003)
33. M. Mudrich, O. Bünerman, F. Stienkemeier, O. Dulieu, M. Weidemüller, Eur. Phys. J. D **31**, 291 (2004)
34. M. DiRosa, abstract for the ITAMP/CUA workshop on Ultracold Polar Molecules, Jan. (2004)
35. L. Santos, G. Shlyapnikov, P. Zoller, M. Lewenstein, Phys. Rev. Lett. **85**, 1791 (2000)
36. B. Damski, L. Santos, E. Tiemann, M. Lewenstein, S. Kotochigova, P. Julienne, P. Zoller, Phys. Rev. Lett. **90**, 110401 (2003)
37. A. Avdeenkov, J. Bohn, Phys. Rev. Lett. **89**, 043006 (2003)
38. D. DeMille, Phys. Rev. Lett. **88**, 067901 (2002)
39. A.R. Allouche, M. Korek, K. Fakherddin, A. Chaalan, M. Dagher, F. Taher, M. Aubert-Frécon, J. Phys. B **33**, 2307 (2000)
40. H. Fahs, A.R. Allouche, M. Korek, M. Aubert-Frécon, J. Phys. B **35**, 1501 (2002)
41. S. Kotochigova, private communication
42. W. Ketterle et al., Phys. Rev. Lett. **70**, 2253 (1993); C.G. Townsend et al., Phys. Rev. A **53**, 1702 (1996)
43. T. Bergeman, C.E. Fellows, R.F. Gutterres, C. Amiot, Phys. Rev. A **67**, 050501R (2003)
44. C.E. Fellows, T. Bergeman, unpublished work
45. C.E. Fellows, R.F. Gutterres, A.P.C. Campos, J. Vergès, C. Amiot, J. Mol. Spectry. **197**, 19 (1999)
46. D. Colbert, W. Miller, J. Chem. Phys. **96**, 1982 (1992)
47. E. Tiesinga, C. Williams, P. Julienne, Phys. Rev. A **57**, 4257 (1998)
48. H. Lefbvre-Brion, R.W. Field, *Perturbations in the Spectra of Diatomic Molecules* (Academic, New York, 1986)
49. Ch. Lisdat, O. Dulieu, H. Knöckel, E. Tiemann, Eur. Phys. J. D **17**, 319 (2001)
50. M.R. Manaa, A. Ross, F. Martin, P. Crozet, A. Lyyra, L. Li, C. Amiot, T. Bergeman, J. Chem. Phys. **117**, 11208 (2002)
51. V. Kokoouline, O. Dulieu, R. Kosloff, F. Masnou-Seeuws, Phys. Rev. A **62**, 032716 (2000)
52. P. G. Hajigeorgiou, R.J. Le Roy, J. Chem. Phys. **112**, 3949 (2000)
53. M. Marinescu, H.R. Sadeghpour, Phys. Rev. A **59**, 390 (1999)
54. J.L. Dunham, Phys. Rev. **41**, 713, 721 (1932)
55. R. Rydberg, Z. Phys. **73**, 326 (1931); O. Klein, Z. Phys. **76**, 226 (1932); A.L.G. Rees, Proc. Phys. Soc. **59**, 998 (1947)
56. M.R. Manaa, Int. J. Quant. Chem. **75**, 693 (1999)
57. R. Ferber, E.A. Pazyuk, A.V. Stolyarov, A. Zaitsevskii, P. Kowalczyk, H. Chen, H. Wang, W.C. Stwalley, J. Chem. Phys. **112**, 5740 (2000)
58. M. Tamanis, R. Ferber, A. Zaitsevskii, E. Pazyuk, A. Stolyarov, H. Chen, J. Qi, H. Wang, W. Stwalley, J. Chem. Phys. **117**, 7980 (2002)
59. O. Dulieu, private communication (2004)